Algorithm for evaluation of temperature distribution of a vapor cell in a diode-pumped alkali laser system: part I

Juhong Han, You Wang,* He Cai, Wei Zhang, Liangping Xue, and Hongyuan Wang

Southwest Institute of Technical Physics, Chengdu, Sichuan 610041, China
**youwang_2007@aliyun.com*

Abstract: A diode-pumped alkali laser (DPAL) is one of the most hopeful candidates to achieve high power performances. As the laser medium is in a gas-state, populations of energy-levels of a DPAL are strongly dependent on the vapor temperature. Thus, the temperature distribution directly determines the output characteristics of a DPAL. In this report, we developed a systematic model by combining the procedures of heat transfer and laser kinetics together to explore the radial temperature distribution in the transverse section of a cesium vapor cell. A cyclic iterative approach is adopted to calculate the population densities. The corresponding temperature distributions have been obtained for different beam waists and pump powers. The conclusion is thought to be useful for realizing a DPAL with high output power.

OCIS codes: (140.1340) Atomic gas lasers; (140.3430) Laser theory; (140.3460) Lasers; (140.3480) Lasers; diode-pumped.

References and links

1. W. F. Krupke, "Diode Pumped Alkali Laser," US Patent Application US 2003/0099272 Al, (2003).
2. W. F. Krupke, R. J. Beach, V. K. Kanz, and S. A. Payne, "Resonance transition 795-nm rubidium laser," Opt. Lett. **28**(23), 2336–2338 (2003).
3. W. F. Krupke, R. J. Beach, S. A. Payne, V. K. Kanz, and J. T. Early, "DPAL: A new class of lasers for CW power beaming at ideal photovoltaic cell wavelengths," 2nd International Symposium on Beamed Energy Propulsion (Japan), (2003).
4. R. H. Page, R. J. Beach, V. K. Kanz, and W. F. Krupke, "Multimode-diode-pumped gas (alkali-vapor) laser," Opt. Lett. **31**(3), 353–355 (2006).
5. Y. Wang, T. Kasamatsu, Y. Zheng, H. Miyajima, H. Fukuoka, S. Matsuoka, M. Niigaki, H. Kubomura, T. Hiruma, and H. Kan, "Cesium vapor laser pumped by a volume-Bragg-grating coupled quasi-continuous-wave laser-diode array," Appl. Phys. Lett. **88**(14), 141112 (2006).
6. B. V. Zhdanov, A. Stooke, G. Boyadjian, A. Voci, and R. J. Knize, "Rubidium vapor laser pumped by two laser diode arrays," Opt. Lett. **33**(5), 414–415 (2008).
7. R. Z. Hua, S. Wada, and H. Tashiro, "Versatile, compact, TEM00-mode resonator for side-pumped single-rod solid-state lasers," Appl. Opt. **40**(15), 2468–2474 (2001).
8. Y. Wang and H. Kan, "Improvement on evaluating absorption efficiency of a medium rod for LD side-pumped solid-state lasers," Opt. Commun. **226**(1-6), 303–316 (2003).
9. Y. Wang, M. Niigaki, H. Fukuoka, Y. Zheng, H. Miyajima, S. Matsuoka, H. Kubomura, T. Hiruma, and H. Kan, "Approaches of output improvement for cesium vapor laser pumped by a volume-Bragg-grating coupled laser-diode-array," Phys. Lett. A **360**(4-5), 659–663 (2007).
10. B. V. Zhdanov and R. J. Knize, "Diode-pumped 10 W continuous wave cesium laser," Opt. Lett. **32**(15), 2167–2169 (2007).
11. W. F. Krupke, "Diode pumped alkali lasers (DPALs)—A review (rev1)," Prog. Quantum Electron. **36**(1), 4–28 (2012).
12. R. J. Beach, W. F. Krupke, V. K. Kanz, S. A. Payne, M. A. Dubinskii, and L. D. Merkle, "End-pumped continuous-wave alkali vapor lasers: experiment, model, and power scaling," J. Opt. Soc. Am. B **21**(12), 2151–2163 (2004).
13. Y. Wang, K. Inoue, H. Kan, T. Ogawa, and S. Wada, "A MOPA with double-end pumped configuration using total internal reflection," Laser Phys. **20**(2), 447–453 (2010).
14. M. Stanghini, M. Basso, R. Genesio, A. Tesi, R. Meucci, and M. Ciofini, "A new three-equation model for the CO_2 laser," IEEE J. Quantum Electron. **32**(7), 1126–1131 (1996).

#210310 - $15.00 USD Received 18 Apr 2014; revised 18 May 2014; accepted 18 May 2014; published 30 May 2014

15. R. J. Garman, "Modelling of the intracavity optical fields in a copper vapour laser," Opt. Commun. **119**(3-4), 415–423 (1995).
16. C. C. Lai, K. Y. Huang, H. J. Tsai, K. Y. Hsu, S. K. Liu, C. T. Cheng, K. D. Ji, C. P. Ke, S. R. Lin, and S. L. Huang, "Yb^{3+}:YAG silica fiber laser," Opt. Lett. **34**(15), 2357–2359 (2009).
17. D. A. Steck, Rubidium 85 D Line Data. Available: *http://steck.us/alkalidata*.
18. C. V. Sulham, G. P. Perram, M. P. Wilkinson, and D. A. Hostutler, "A pulsed, optically pumped rubidium laser at high pump intensity," Opt. Commun. **283**(21), 4328–4332 (2010).
19. Z. N. Yang, H. Y. Wang, Q. S. Lu, W. H. Hua, and X. J. Xu, "Modeling of an optically side-pumped alkali vapor amplifier with consideration of amplified spontaneous emission," Opt. Express **19**(23), 23118–23131 (2011).
20. Q. Zhu, B. L. Pan, L. Chen, Y. J. Wang, and X. Y. Zhang, "Analysis of temperature distributions in diode-pumped alkali vapor lasers," Opt. Commun. **283**(11), 2406–2410 (2010).
21. Y. F. Liu, B. L. Pan, J. Yang, Y. J. Wang, and M. H. Li, "Thermal Effects in High-Power Double Diode-End-Pumped Cs Vapor Lasers," IEEE J. Quantum Electron. **48**(4), 485–489 (2012).
22. B. D. Barmashenko and S. Rosenwaks, "Modeling of flowing gas diode pumped alkali lasers: dependence of the operation on the gas velocity and on the nature of the buffer gas," Opt. Lett. **37**(17), 3615–3617 (2012).
23. B. D. Barmashenko and S. Rosenwaks, "Feasibility of supersonic diode pumped alkali lasers: Model calculations," Appl. Phys. Lett. **102**(14), 141108 (2013).
24. B. D. Barmashenko and S. Rosenwaks, "Detailed analysis of kinetic and fluid dynamic processes in diode-pumped alkali lasers," J. Opt. Soc. Am. B **30**(5), 1118–1126 (2013).
25. S. Rosenwaks, B. D. Barmashenko and Waichman, "Semi-analytical and 3D CFD DPAL modeling: feasibility of supersonic operation", Proc. SPIE 8962, High Energy/Average Power Lasers and Intense Beam Applications VII, **896209**, 1–9 (2014).
26. S. Kiwan and O. Zeitoun, "Natural convection in a horizontal cylindrical annulus using porous fins," Int. J. Numer. Methods Heat Fluid Flow **18**(5), 618–634 (2008).
27. P. Teerstra and M. M. Yovanovich, " Comprehensive review of natural convection in horizontal circular annuli," in 7th AIAA/ ASME Joint Thermophysics and Heat Transfer Conference, Albuquerque, New Mexico, 15 –18 June 1998 (AIAA, 1998), pp. 141–152.
28. Z. N. Yang, H. Y. Wang, Q. S. Lu, Y. D. Li, W. H. Hua, X. J. Xu, and J. B. Chen, "Modeling, numerical approach, and power scaling of alkali vapor lasers in side-pumped configuration with flowing medium," J. Opt. Soc. Am. B **28**(6), 1353–1364 (2011).
29. S. W. Smith, *The Scientist and Engineer's Guide to Digital Signal Processing[J]*, II ed, (California Technical Publishing, 1999), Chapter 25.
30. D. A. Steck, "Cesium D line data," Available: *http://steck.us/alkalidata*
31. M. J. Latif, *Heat Conduction*, III ed., (Verlag Berlin and Heidelberg GmbH & Co. K, 2009), Chapter 1,.
32. C. L. Yaws, *Matheson Gas Data Book,* VII ed., (McGraw-Hill & Matheson Tri-Gas, 2001), Appendix 23.
33. H. Cai, Y. Wang, W. Zhang, L. P. Xue, H. Y. Wang, J. H. Han, and Z. Y. Liao, "Characteristic analyses of a diode-pumped rubidium vapor laser using a kinetic algorithm," Opt. & Laser Technol., to be submitted.
34. N. D. Zameroski, G. D. Hager, W. Rudolph, and D. A. Hostutler, "Experimental and numerical modeling studies of a pulsed rubidium optically pumped alkali metal vapor laser," J. Opt. Soc. Am. B **28**(5), 1088–1099 (2011).

1. Introduction

Since W. F. Krupke in Lawrence Livermore National Laboratory (LLNL) invented the diode-pumped alkali laser (DPAL) at the beginning of the 21th century, such a new type of laser has been rapidly developed in the last decade [1–3].

In fact, DPALs combine the major advantages of solid-state lasers and gas-state lasers and obviate their main disadvantages at the same time [4–6]. Comparing to the traditional diode-pumped solid-state laser (DPSSL), DPALs have high Stokes Efficiency, good thermal performance, narrow linewidth, compact size, non-toxic system, etc [7–11]. Generally, the collisionally broadened cross sections of both the D_1 and D_2 lines are of the order of 10^{-13} cm^{-2} at 110 °C [12]. Such values are much larger than the cross sections of stimulated radiation for the most conventional solid-state, fiber and gas lasers (e.g., about 10^6 times larger than a Nd:YAG laser) [13–16]. Thus, DPALs provide an outstanding potentiality for realization of high-powered laser systems. With so many marvelous merits, a DPAL becomes one of the most hopeful high-powered laser sources of next generation.

Unlike other types of lasers, the density of a gain medium inside a vapor cell is extremely sensitive to the ambient temperature [17–19]. When the pump power for a DPAL is small enough, heat generated in the vapor cell provides almost no effects on laser properties and is usually neglected. However, when a high-powered diode is used to pump the vapor cell, the

#210310 - $15.00 USD Received 18 Apr 2014; revised 18 May 2014; accepted 18 May 2014; published 30 May 2014

laser features might become somewhat strange, and some physical characteristics, e.g. the transverse gain distribution, might be different from those for an ordinary solid-state laser.

Therefore, there is a necessity for DPAL technicians to investigate generated heat as well as the temperature distribution in the vapor cell for construction of a DPAL system with high beam quality. One of the greatest difficulties for examination of thermal characteristics of a DAPL cell is that the population status exhibits an inhomogeneous distribution due to the temperature gradient inside an alkali cell. Simultaneous evaluations of both the population and the temperature distributions cannot be simply completed only with the analyses of thermal conductivity or kinetic calculations. Until now, two teams have carried out studies on the temperature distribution inside an alkali vapor cell. One is the team headed by B. L. Pan, whose interests concentrate on the heat transfer and the optical path difference (OPD) under different pump powers [20, 21]. They calculated the temperature distribution by using an assumed absorption coefficient, and the lasing process was not taken into account in their scheme. The other is B. D. Barmashenko's team and their calculation model was only based on the kinetic evaluation while the temperature distribution was not discussed [22–25]. In their model, the temperature is assumed as a constant inside the lasing region.

To deduce an accurate temperature distribution inside a vapor cell, it is essential to create an analytic system by considering both the laser kinetics and the heat transfer. In our report, the heat generating dynamics and heat transfer are investigated by two interrelated theoretical procedures. The results reveal that the radial temperature gradient inside the vapor cell cannot be simply ignored for a real DPAL. To the best of our knowledge, there have not been any similar reports on this topic so far.

2. Theory and method

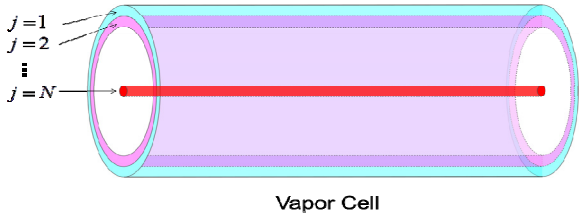

Fig. 1. Schematic illustration of a segmented configuration of a vapor cell.

For an end-pumped configuration, the optical axis of a pump laser diode coincides with that of a DPAL. As shown in Fig. 1, we divide a cylindrical vapor cell into many cylindrical annuli whose axes are same. Every cylindrical annulus is thought as a heat source. These coaxial cylindrical annuli will be used in the segmental accumulation procedure as introduced next.

During the evaluation, we made the following assumptions:

(1) The diameter of the DPAL beam is approximately treated to be unchanged along the optical axis;

(2) The transverse pump distribution holds out a Gaussian intensity profile and keeps unchanged along the optical axis;

(3) The temperature of every cylindrical annulus is a constant along the optical axis;

(4) The effects of both end-windows of the enclosed vapor cell are ignored.

Actually, the variations in diameter of both the DPAL and the pump beams are very tiny inside a 2.5cm-long cell. For example, the variation of the beam size is only about 2.2% for a pump beam with the waist size of 150 μm. In this research, the temperature distribution along the axial direction is ignored with purpose of the algorithm simplification. We will undertake the evaluation of an enclosed cell to deduce the realistic 3-dimensional temperature

#210310 - $15.00 USD Received 18 Apr 2014; revised 18 May 2014; accepted 18 May 2014; published 30 May 2014

distribution, in which the effects of both end-windows are taken into account in the evaluation regime.

Heat transfer in a gas-state medium exhibits three types: heat radiation, convection, and conduction. Since the thickness of every cylindrical annulus is very small, heat transfer between the annulus gap is mainly dominated by heat conduction and the effects of natural convection is neglected in such a narrow gap [26, 27]. Additionally, heat radiation is so small that it can also be ignored here.

2.1. Analyses of laser kinetics

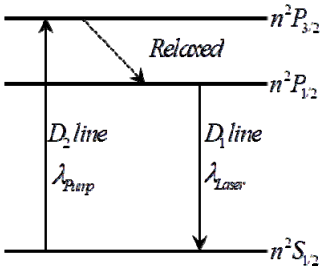

Fig. 2. Diagram of energy levels of an alkali atom.

Generally, a DPAL is thought to be a typical three-level laser source with a tiny quantum defect. As shown in Fig. 2, the stimulated radiation transition $n^2P_{1/2} \rightarrow n^2S_{1/2}$ is called D_1 line and the stimulated absorption transition (pump transition) $n\ ^2S_{1/2} \rightarrow n\ ^2P_{3/2}$ is called D_2 line, where n = 4, 5 and 6 for K, Rb and Cs, respectively [12]. The D_2 line can be collisionally broadened to achieve spectrally homogeneous transition by using a buffer gas such as helium. In the presence of helium buffer gas, the D_2 pump transition line-shape changes from Gaussian to Lorentzian. Thus, pump energy absorbed in the spectral wings of the pump transition can dramatically enhance the laser gain by comparing the case of no helium buffer gas. The effectively collision-broadened linewidth is generally at least ten times the Doppler linewidth. The relaxation rate of the fine-structure can be enhanced by adding some alkanes with small hydrocarbon molecules [18, 19, 28]. In the theoretical simulation of this report, we choose cesium as the laser gain medium, and helium and ethane as buffer gases.

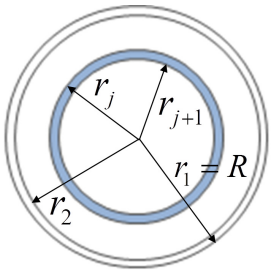

Fig. 3. Transverse view of a vapor cell.

As shown in Fig. 3, we select an arbitrarily cylindrical annulus (*jth*) among the segments. The outside radius r_j and the inner radius r_{j+1} of this cylindrical annulus can be simply expressed by

$$\begin{aligned} r_j &= R-(j-1)\bullet R/N \quad , \\ r_{j+1} &= R-j\bullet R/N \quad . \end{aligned} \tag{1}$$

where R is the radius of a vapor cell, N is the total number of segmented cylindrical annuli, respectively.

#210310 - $15.00 USD Received 18 Apr 2014; revised 18 May 2014; accepted 18 May 2014; published 30 May 2014

Next, we calculate the population distribution in the three energy-level system of the *jth* cylindrical annulus (see Fig. 3) by using the well-known rate equations as follows [12]:

$$\begin{aligned}
\frac{dn_1^j}{dt} &= -\Gamma_p^j + \Gamma_L^j + \frac{n_2^j}{\tau_{D_1}} + \frac{n_3^j}{\tau_{D_2}} \quad , \\
\frac{dn_2^j}{dt} &= -\Gamma_L^j + \gamma_{32}\left(T_j\right)\left[n_3^j - 2n_2^j \exp\left(-\frac{\Delta E}{k_B T_j}\right)\right] - \frac{n_2^j}{\tau_{D_1}} \quad , \\
\frac{dn_3^j}{dt} &= \Gamma_p^j - \gamma_{32}\left(T_j\right)\left[n_3^j - 2n_2^j \exp\left(-\frac{\Delta E}{k_B T_j}\right)\right] - \frac{n_3^j}{\tau_{D_2}} \quad ,
\end{aligned} \tag{2}$$

where k_B is the Boltzmann constant, τ_{D_1} is the D_1 radiative lifetime, τ_{D_2} is the D_2 radiative lifetime, ΔE is the energy gap between the $^2P_{3/2}$ and the $^2P_{1/2}$ states, T_j is the temperature of the *jth* cylindrical annulus, $\gamma_{32}(T_j)$ is the fine-structure relaxation rate as given by

$$\gamma_{32}\left(T_j\right) = n_{\text{ethane}}\sigma_{32}^{\text{ethane}} v_r^{Cs-ethane}\left(T_j\right) + n_{\text{He}}\sigma_{32}^{He} v_r^{Cs-He}\left(T_j\right) \quad , \tag{3}$$

where n_{ethane} is the number density of ethane in the cell, $\sigma_{32}^{\text{ethane}}$ is the ethane cross-section with the value of 5.2×10^{-15} cm^2, σ_{32}^{He} is the cross-section with the value for He with the value of 2.25×10^{-19} cm^2, $v_\gamma^{Cs\text{-He}}(T_j)$ and $v_\gamma^{Cs\text{-ethane}}(T_j)$ are respectively the root mean square thermally averaged relative velocities between cesium atoms and He atoms as well as ethane molecules as given by [12]

$$\begin{aligned}
v_\gamma^{ethane}(T_j) &= \sqrt{3k_B T_j\left(\frac{1}{m_{Cs}} + \frac{1}{m_{ethane}}\right)} \quad , \\
v_\gamma^{He}(T_j) &= \sqrt{3k_B T_j\left(\frac{1}{m_{Cs}} + \frac{1}{m_{He}}\right)} \quad ,
\end{aligned} \tag{4}$$

where m_{Cs}, m_{He} and m_{ethane} are qualities of a cesium atom, a helium atom and an ethane molecule, respectively. Γ_P^j is the stimulated absorption transition rate caused by pump photons as given by [12]

$$\begin{aligned}
\Gamma_P^j = \frac{\eta_{del}}{V_L^j}\int \frac{\lambda}{hc} P_j(\lambda) \times &\left\{1 - \exp\left[-\left(n_1^j - \frac{1}{2}n_3^j\right)\sigma_{D_2}\left(T_j,\lambda\right)l\right]\right\} \\
\times &\left\{1 + R_P \exp\left[-\left(n_1^j - \frac{1}{2}n_3^j\right)\sigma_{D_2}\left(T_j,\lambda\right)l\right]\right\} \quad ,
\end{aligned} \tag{5}$$

where η_{del} is the fraction of the pump power delivered from the pump excitation source to the input end of the laser gain medium, R_P is the reflectance of the pump light at the output coupler of a laser cavity resonator, V_L^j is the volume of the *jth* cylindrical annulus as given by

$$V_L^j = \pi\left(r_j^2 - r_{j+1}^2\right)l \quad , \tag{6}$$

$P_j(\lambda)$ is the spectrally resolved partial pump power of the *jth* cylindrical annulus as expressed by [29]

#210310 - $15.00 USD Received 18 Apr 2014; revised 18 May 2014; accepted 18 May 2014; published 30 May 2014

$$P_j(\lambda) = \frac{P_j^{peak}}{\sqrt{2\pi(\Delta\lambda_{D_2}^{FWHM}/2\sqrt{2\ln 2})^2}} \exp\left(-\frac{(\lambda-\lambda_0)^2}{2(\Delta\lambda_{D_2}^{FWHM}/2\sqrt{2\ln 2})^2}\right) \quad , \tag{7}$$

where $\Delta\lambda_{D_2}^{FWHM}$ is the spectrally resolved FWHM linewidth, P_j^{peak} is the peak pump power of the *jth* cylindrical annulus as given by

$$\begin{aligned} P_j^{peak} &= \int I_j(r)\, dS \\ &\approx S_j \cdot I_{\max} \exp\left(-\frac{2r_j^2}{\omega_P^2}\right) \end{aligned} \quad , \tag{8}$$

where $I_j(r)$ is the intensity distribution of the pump power of the *jth* cylindrical annulus, r is the radius at the cross-section, ω_P is the pump waist radius, S_j is the cross-section area of the *jth* cylindrical annulus:

$$S_j = \pi\left(r_j^2 - r_{j+1}^2\right) \quad . \tag{9}$$

The maximal intensity of the pump power of the *jth* cylindrical annulus $I_{\max}$ can be calculated by

$$\begin{aligned} I_{\max} &= \frac{P_P}{\int \exp\left(-\frac{2r^2}{\omega_P^2}\right) dS} \\ &= \frac{P_P}{\int_0^R \exp\left(-\frac{2r^2}{\omega_P^2}\right) \cdot 2\pi r\, dr} \\ &\approx \frac{P_P}{\sum_{j=1}^{N} \exp\left(-\frac{2r_j^2}{\omega_P^2}\right) \cdot S_j} \end{aligned} \quad . \tag{10}$$

$\sigma_{D_2}(T_j, \lambda)$ is the pump absorption cross-section as expressed by [12]

$$\sigma_{D_2}(T_j, \lambda) = \frac{\sigma_{D_2}^{He-broadened}(T_j)}{1 + \left(\frac{\lambda - \lambda_{D_2}}{\Delta\lambda_{D_2}^{FWHM}/2}\right)^2} \quad , \tag{11}$$

where

$$\sigma_{D_2}^{He-broadened}(T_j) = \frac{\sigma_{D_2}^{radiative}}{2\pi\tau_{D_2} n_{He-amagat}\left(19.3\frac{GHz}{amagat}\right)\sqrt{\frac{T_j}{294\ K}}} \quad , \tag{12}$$

where $n_{He\text{-}amagat}$ is the number density of helium in the vapor cell, $\sigma_{D_2}^{radiative}$ is the atomic cross section of the D_2 line with the value of 2.31×10^{-9} cm^2, respectively. Γ_L^j is the transition rate of laser emission as expressed by [12]

#210310 - $15.00 USD Received 18 Apr 2014; revised 18 May 2014; accepted 18 May 2014; published 30 May 2014

$$\Gamma_L^j = \begin{cases} \dfrac{1}{V_L^j}\dfrac{P_L^j}{h\upsilon_L}\dfrac{R_{oc}}{1-R_{oc}}\times\left\{\exp\left[\left(n_2^j-n_1^j\right)\sigma_{D_1}^{He-broadened}\left(T_j\right)l\right]-1\right\} \\ \qquad\times\left\{1+TT^2\exp\left[\left(n_2^j-n_1^j\right)\sigma_{D_1}^{He-broadened}\left(T_j\right)l\right]\right\}\ ,\ with\ \ laser\ output \\ 0\ , \qquad without\ \ laser\ output \end{cases} \quad , \tag{13}$$

where P_L^j is the output alkali laser power, R_{oc} is the reflectance of the output coupler, and TT is the one-way cavity transmittance by neglecting the ground-state absorption as well as the output coupler loss. $\sigma_{D_1}^{He-broadened}(T_j)$ is collisionally-broadened cross section as given by [12]

$$\sigma_{D_1}^{He-broadened}(T_j) = \frac{\sigma_{D_1}^{radiative}}{2\pi\tau_{D_1}n_{He-amagat}\left(21.5\dfrac{GHz}{amagat}\right)\sqrt{\dfrac{T_j}{294\ K}}} \quad , \tag{14}$$

where $\sigma_{D_1}^{radiative}$ is the atomic cross section of the D_1 line.

In addition, the number density of every energy-level must satisfy the following two equations for a steady-state laser emission [12]:

$$\exp\left[2\left(n_2^j\left(T_j\right)\text{-}n_1^j\left(T_j\right)\right)\sigma_{\mathrm{D_1}}^{\text{He-broadened}}\left(T_j\right)l\right]\times TT^2\cdot R_{oc}=1 \quad , \tag{15}$$

$$n_0^j\left(T_j\right)=n_1^j\left(T_j\right)+n_2^j\left(T_j\right)+n_3^j\left(T_j\right) \quad , \tag{16}$$

where $n_0^j(T_j)$ is the total alkali number density of the *jth* cylindrical annulus as expressed by [22]

$$n_0^j(T_j) = \begin{cases} n_0^1(T_w)\ , & j=1 \\ n_0^1(T_w)\left(\dfrac{T_w}{T_j}\right)\ , & j>1 \end{cases} \quad , \tag{17}$$

where T_w is the temperature of the cell wall, $n_0^1(T_w)$ is the saturated alkali number density inside the first cylindrical annulus which is adjacent to the inner surface cell wall as given by [30]

$$n_0^1(T_w) = \frac{133.322N_A}{RT_w}\left(10^{\,8.22127-\frac{4006.048}{T_w}-0.00060194T_w-0.19623\log_{10}T_w}\right) \quad , \tag{18}$$

where R is a constant of proportionality with the value of 8.3143 *J/(mol·K),* P_V is the saturation pressure of the cesium vapor in *Torr* and N_A is Avogadro number, respectively.

Next, we calculate the volume density of generated heat of the *jth* cylindrical annulus by using the following formula [12]:

$$\Omega_j = \gamma_{32}\left(T_j\right)[n_3^j-2n_2^j\exp(-\frac{\Delta E}{k_BT_j})]\Delta E \quad , \tag{19}$$

where ΔE is the energy gap between 6 $^2S_{1/2}$ and 6 $^2P_{3/2}$ levels with the value of 554 cm^{-1}.

#210310 - $15.00 USD Received 18 Apr 2014; revised 18 May 2014; accepted 18 May 2014; published 30 May 2014

Thus, the generated heat of the *jth* cylindrical annulus can be obtained by the following calculation:

$$Q_j = V_L^i \cdot \Omega_j \quad . \tag{20}$$

2.2. Theoretical analyses of heat transfer

2.2.1. Calculation of a Transverse Section Except the Central Core

Generally, the differential equation of thermal conductivity in the cylindrical coordinate system is given by [31]

$$\frac{d}{dr}\left(r\frac{dT}{dr}\right)+\frac{\Omega \cdot r}{K(T)}=0 \quad , \tag{21}$$

where Ω stands for the volume density of generated heat and $K(T)$ denotes the coefficient of thermal conductivity, respectively. When the thickness of the segmented cylindrical annulus is small enough, the volume density of the *jth* cylindrical annulus can be approximately expressed as of the volume density Ω_j at the exterior side of the cylindrical annulus (*j = 1, 2, ... (N-1)*). Similarly, $K(T)$ can also be approximately expressed as $K(T_j)$, which is the thermal conductivity at the exterior side of the *jth* cylindrical annulus as expressed by [24]

$$K(T_j)=\frac{P_{He}}{P_{He}+P_{C_2H_6}}K_{He}(T_j)+\frac{P_{C_2H_6}}{P_{He}+P_{C_2H_6}}K_{C_2H_6}(T_j) \quad , \tag{22}$$

where P_{He} and $P_{C_2H_6}$ are respectively the partial pressures of helium and ethane. $K_{He}(T_j)$ and $K_{He}(T_j)$ are respectively the thermal conductivities of helium and ethane as given by [32]

$$\begin{aligned} K_{He}(T_j) &= 0.05516+3.2540\times10^{-4}T_j-2.2723\times10^{-8}T_j^2 \quad , \\ K_{C_2H_6}(T_j) &= -0.01936+1.2547\times10^{-4}T_j+3.8298\times10^{-8}T_j^2 \quad . \end{aligned} \tag{23}$$

Next, we get the following formula by undertaking the integral calculation on both sides of Eq. (21):

$$\frac{dT}{dr}+\frac{\Omega_j \cdot r}{2K(T_j)}=\frac{C_j^1}{r} \quad , \tag{24}$$

where C_j^1 is a constant for the *jth* cylindrical annulus. According to Fourier's Law, the quantity of the transferred heat Φ_j from the *jth* cylindrical annulus to the *(j-1)th* one can be expressed by [31]

$$\Phi_j=\left[-K(T)\cdot A\frac{dT}{dr}\right]\Bigg|_{T=T_j} \quad , \tag{25}$$

where A stands for the lateral area of the *jth* cylindrical annulus as given by

$$A=2\pi r_j l \quad , \tag{26}$$

where l is the cell length. After substituting Eqs. (24) and (26) into Eq. (25), C_j^1 can be calculated by the following formula:

#210310 - $15.00 USD Received 18 Apr 2014; revised 18 May 2014; accepted 18 May 2014; published 30 May 2014

$$C_j^1 = \frac{\Omega_j \cdot r_j^2}{2K(T_j)} - \frac{\Phi_j \cdot r_j}{K(T_j) \cdot A_j} \quad . \tag{27}$$

Note Ω_j is calculated by use of Eq. (18) of Subsection 2.1. Then, we make a further integral calculation on both sides of Eq. (24) and the temperature distribution inside the *jth* cylindrical annulus can be given by

$$T(r) = C_j^1 \ln r - \frac{\Omega_j \cdot r^2}{4K(T_j)} + C_j^0 \quad , \tag{28}$$

where C_j^0 is another constant for the *jth* cylindrical annulus which can be solved by substituting $r = r_j$ and $T = T_j$ into Eq. (28):

$$C_j^0 = T_j - C_j^1 \ln r_j + \frac{\Omega_j \cdot r_j^2}{4K(T_j)} \quad . \tag{29}$$

By substituting C_j^1 and C_j^0 into Eq. (28), one can obtain the temperature distribution in the transverse section of the *jth* cylindrical annulus. The temperature of the inner side of the *jth* cylindrical annulus, T_{j+1}, can also be deduced and is then used as the board condition in the calculation of the *(j + 1)th* cylindrical annulus. By employing a circulatory calculation, we can therefore obtain T_2, T_3, ..., T_N.

2.2.2. Calculation of Temperature of the Central Core

The exterior radius r_N of the central cylinder (core) can be simply expressed by

$$r_N = R / N \quad , \tag{30}$$

We can calculate out $C_N^1 = 0$ by substituting the boundary condition $\left.\frac{dT}{dr}\right|_{r=0} = 0$ into Eq. (24) .Then we simplify Eq. (24) as the following style:

$$\frac{dT}{dr} + \frac{\Omega_N \cdot r}{2K(T_N)} = 0 \quad . \tag{31}$$

The temperature distribution inside the central core can be given by

$$T(r) = -\frac{\Omega_N \cdot r^2}{4K(T_N)} + C_N^0 \quad , \tag{32}$$

C_N^0 can be solved by substituting $r = r_N$, $T = T_N$ into Eq. (32),

$$C_N^0 = T_N + \frac{\Omega_N \cdot r_N^2}{4K(T_N)} \quad . \tag{33}$$

The central temperature of the vapor cell, T_{N+1}, can be obtained by substituting $r = 0$ into Eq. (32). By combing the results of Eqs. (28) and (32) together, it is possible to acquire the whole temperature distribution at the cross-section of the vapor cell.

#210310 - $15.00 USD Received 18 Apr 2014; revised 18 May 2014; accepted 18 May 2014; published 30 May 2014

2.3. Calculation of radial temperature distribution

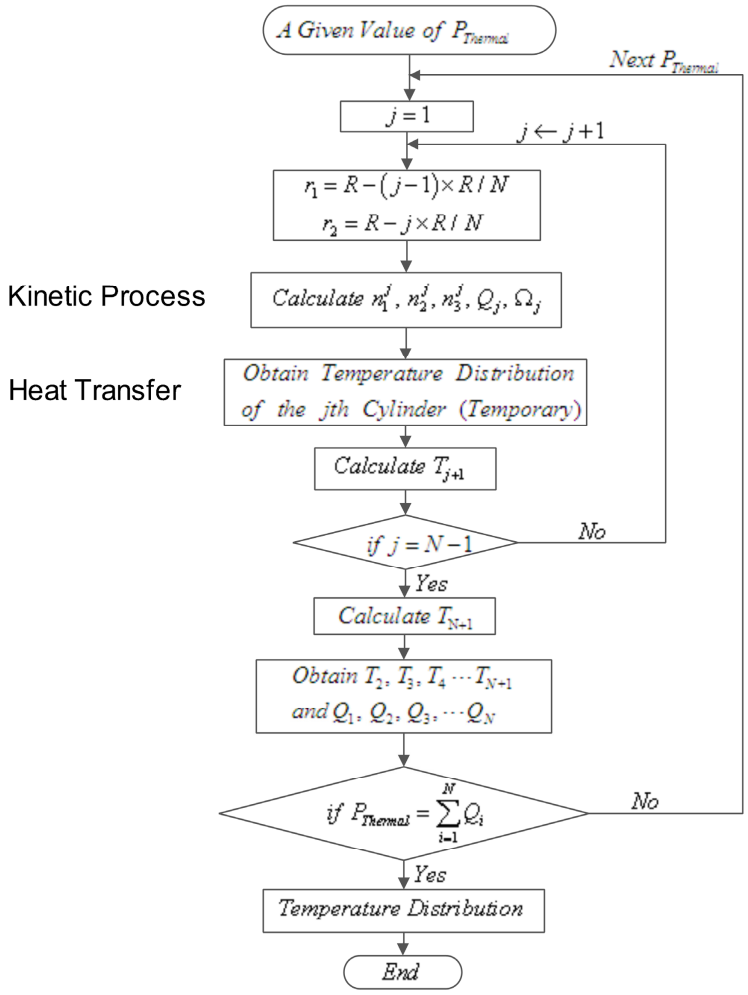

Fig. 4. Flowchart of evaluating the distributions of temperature and population of a vapor cell.

The flowchart for evaluation of the temperature distribution is diagramed in Fig. 4. First, we assume that the total heat transferred out from a vapor cell is $P_{Thermal}$. By considering a fact that the heat delivered from the first cylindrical annulus to the cell wall, Φ_1, is equal to the total heat release, the following relationship is tenable:

$$\Phi_1 = P_{Thermal} \quad . \tag{34}$$

The temperature at the outside of the first cylindrical annulus, which is equal to T_w in this case, is approximately assigned as the temperature of this cylindrical annulus during the kinetic calculation if the thickness of the segmented thickness is small enough. Therefore, the volume heat density Ω_1 as well as the generated heat Q_1 can be deduced by employing the approach introduced in Subsection 2.1. By using Φ_1 and Ω_1, we can evaluate the temperature distribution inside the first cylindrical annulus with Eq. (28).

The temperature of the inner side of the first cylindrical annulus, T_2, can be then evaluated and is utilized as the initial conditions in calculating the temperature distribution of the second cylindrical annulus. As depictured in Fig. 5, the heat transferred from the second cylindrical annulus to the first one, Φ_2, is thus calculated by

#210310 - $15.00 USD Received 18 Apr 2014; revised 18 May 2014; accepted 18 May 2014; published 30 May 2014

$$\Phi_2 = \Phi_1 - Q_1 = P_{Thermal} - Q_1 \quad . \tag{35}$$

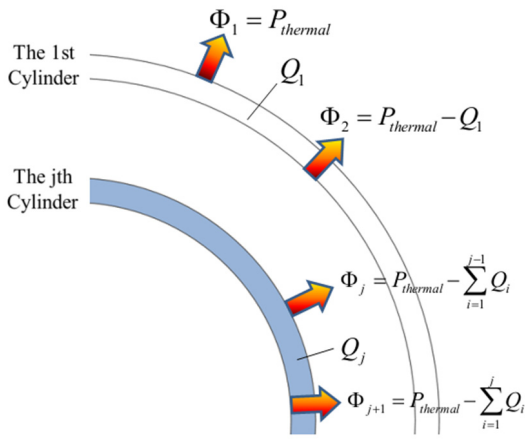

Fig. 5. Drawing of illustrating heat generated and transferred for the first cylindrical annulus and the *jth* cylindrical annulus of a vapor cell.

Therefore, through a circulatory calculation of Q_1, Q_2, ..., Q_{N-1}, we can obtain heat transferred from the *jth* cylindrical annulus to the *(j-1)th* one as expressed by

$$\Phi_j = P_{Thermal} - \sum_{i=1}^{j-1} Q_i \quad , \tag{36}$$

where $j = 1, 2, \ldots, N$.

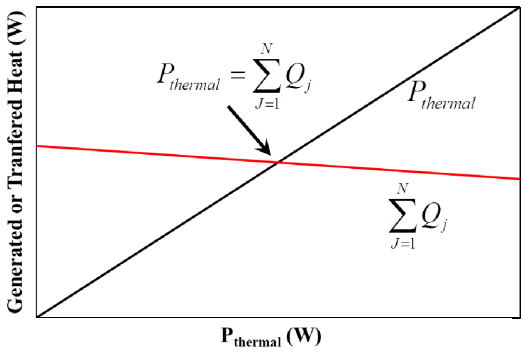

Fig. 6. Sketch for determining the value of $P_{Thermal}$.

Next, we judge whether $\sum_{j=1}^{N} Q_j$ is equal to the given value of $P_{Thermal}$ or not. If the answer is "*no*", the evaluation will be repeated by using the next value of $P_{Thermal}$ until the following equation is satisfied (see Fig. 6):

$$P_{Thermal} = \sum_{j=1}^{N} Q_j \quad . \tag{37}$$

The y-axis in Fig. 6 represents the heat generated from all cylindrical annulii or the heat transferred outside from the first cylindrical annulus. By using the correct value $P_{Thermal}$, the temperature distribution of the vapor cell can be obtained in the transverse section.

#210310 - $15.00 USD Received 18 Apr 2014; revised 18 May 2014; accepted 18 May 2014; published 30 May 2014

3. Results and discussions

3.1. Population distributions

3.1.1. Different waists of pump beams

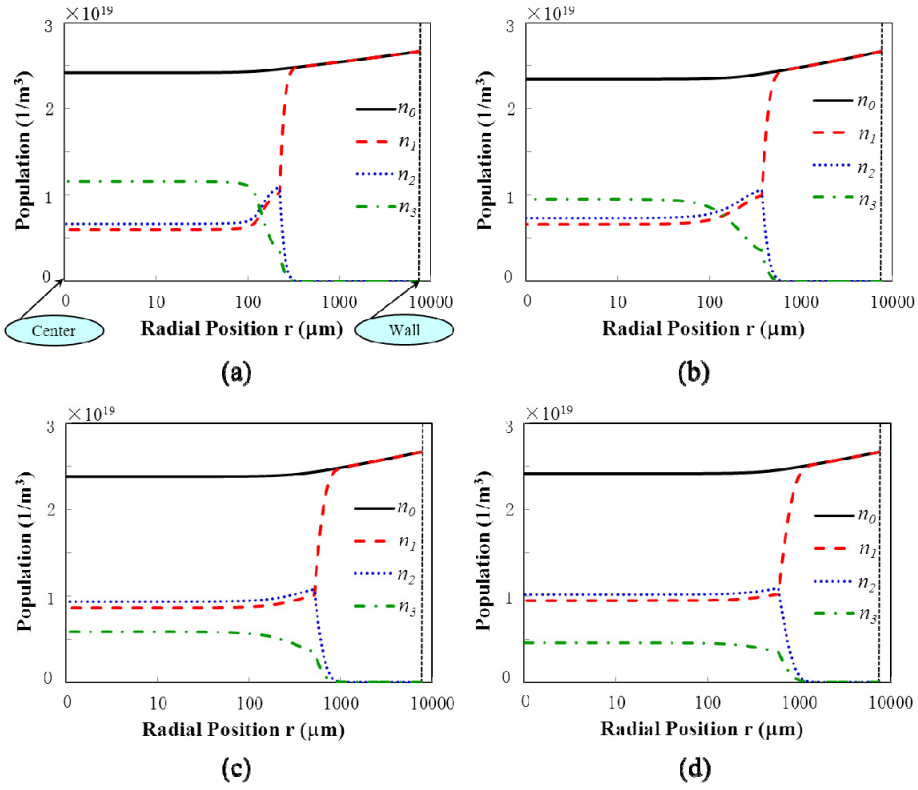

Fig. 7. Population distributions with different waists of a pump beam. The waist radii are 150 μm (a), 300 μm (b), 500 μm (c) and 700 μm (d), respectively.

We first analyze the population distributions inside a cesium vapor cell for different waists of pump beams. By using the approach introduced in Section 2, we calculate the population density distributions inside the cell as illustrated in Fig. 7. During the evaluation, the pump power is fixed to 10 W and the other parameters are listed in Table 1. The waist radii are assumed as 150 μm, 300 μm, 500 μm, and 700 μm corresponding to (a), (b), (c), and (d) in Fig. 7, respectively. It is observed that the total density of the cesium vapor n_0 increases with the radial position r. Such a phenomenon is due to the fact that the temperature at the central area is higher than that near the wall of the vapor cell. Some significant variation of the population densities n_1 and n_2 can be seen in the figure. The inflection points in the legend give rise to discontinuity of the first derivative or "angles" on the curves for n_1 and n_2. Such inflection points located in the lasing boundary line. In the lasing region, n_2 is always larger than n_1 because of population inversion. We also find that, the bigger the spot size of a pump beam is, the lower n_3 becomes. It means that more electrons will be stimulated into the 6 $^2P_{3/2}$ level under a higher pump density. However, it also leads to a population accumulation at the top energy-level. One can realize that the higher pump density brings about a relative weak relaxing capability by comparing n_3 and n_2 in (a), (b), (c), and (d) of Fig. 7.

#210310 - $15.00 USD Received 18 Apr 2014; revised 18 May 2014; accepted 18 May 2014; published 30 May 2014

Table 1. Parameters for evaluating temperature distribution of a Cs vapor cell

Parameter Description	Values
Partial pressure of He	478.8 Torr (0.63 atm)
Partial pressure of C_2H_6	100 Torr
η_{del}	90%
L	25 mm
R	7.5 mm
T_W	383 K
$\sigma_{D_2}^{radiative}$	1.53×10^{-13} m^2
$\sigma_{D_2}^{radiative}$	2.31×10^{-13} m^2
R_{oc}	30%
TT	99%
Pump FWHM	30 GHz
Pump center wavelength	852.3 nm
D_1 transition wavelength	894.6 nm
τ_{D_1}	34.9 ns
τ_{D_2}	30.5 ns

3.1.2. Different pump power

Next, we discuss the population distributions inside a cesium vapor cell for different pump power when the beam waist radius is fixed to 500 μm. By using the method mentioned above, we get the results when the pump power is 1 W, 20 W and 50 W, respectively. As diagramed in Fig. 8, the total number population n_0 decreases with the pump power. The reason is that the central temperature increases with the pump power and the total population density generally exhibits a degressive tendency with the temperature rising by referring Eq. (17). In the calculation, lasing output corresponding to the population distribution in Fig. 8(a) cannot be achieved because the threshold condition is unsatisfied.

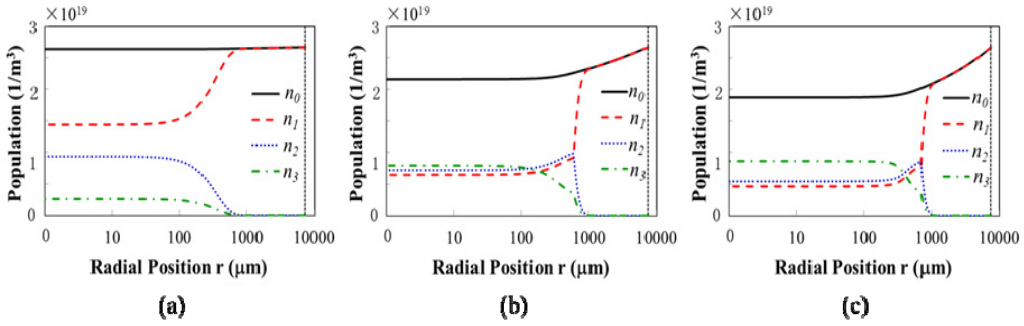

Fig. 8. Population distributions with the pump power of 1 W (a), 20 W (b) and 50 W (c), respectively.

#210310 - $15.00 USD Received 18 Apr 2014; revised 18 May 2014; accepted 18 May 2014; published 30 May 2014

3.2. Temperature distributions

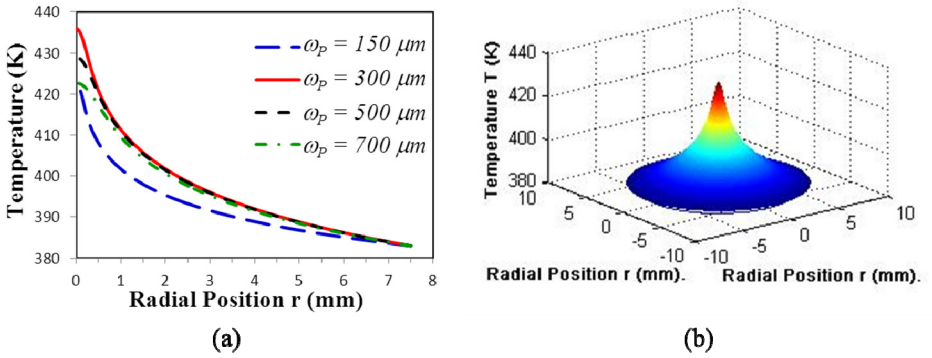

Fig. 9. (a) Temperature distributions with the waist of a pump beam of 150, 300, 500 and 700 μm, respectively. (b) 3-dmensional diagram for ω_p = 500 μm.

By use of the approach introduced in Section 2, the radial temperature distributions are obtained. As shown in Fig. 9, the temperature at the cross section exhibits a distinct gradient and achieves the maximum values at the central axis for every case. Note that the waist radius of the pump beam in Fig. 9(a) is 150, 300, 500 and 700 μm, respectively, when the pump power is set to 10 W. We can observe that the curve for ω_p = 500 μm is almost located at the lowest position at the diagram. It means that a big pump density will not always cause a high heat generation. To make the expression clear, we also produced a 3-Dmensional drawing for ω_p = 500 μm as depictured in Fig. 9(b). In Fig. 10, the pump powers is set to 1, 10, 100, and 500 W, respectively, when the waist radius of the pump beam is 500 μm. It is obvious that the temperature gradient increases rapidly with the pump power. Such tendencies can be explained by a fact that the thermal conductivity of a gas-state medium is so small that the generated heat cannot be transferred outside efficiently.

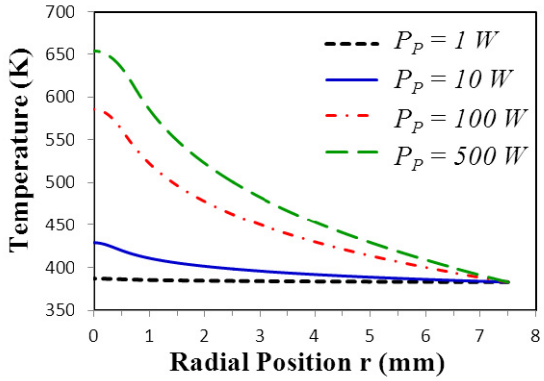

Fig. 10. Temperature distributions with the pump power of 1, 10, 100 and 500 W, respectively.

In Fig. 10, it is easily found that a higher pump power will cause a more distinct temperature gradient. According to our previous study [33] and the experimental results in Ref. 34, there should be an optimum temperature for achieving the highest laser output. Therefore, investigating how the conversion efficiency changes with the pump power becomes a valuable business. In Fig. 11(a), both the absorbed power and the generated heat inside a cesium vapor cell are given as a function of the pump power. Both quantities monotonically increase with the pump level and only less than 5% of the absorption converts to heat. In Fig. 11(b), the optical-optical conversion efficiency first raises as the pump power

#210310 - $15.00 USD Received 18 Apr 2014; revised 18 May 2014; accepted 18 May 2014; published 30 May 2014

increases, and then it gradually slows down. This is because that n_3 becomes higher in this case, and decrease in the population densities n_1 and n_2 will lead to a relatively low conversion efficiency.

It is interesting to find that the peak position of the optical-optical conversion efficiency corresponds to a relatively low output. The optimum pump power is around 30 W for the optical-optical conversion efficiency but the laser output is only 13.4 W. The results are different from some traditional solid-state lasers. Thus, the output characteristics of a DPAL are not only dependent on the energy levels, but also determined by the thermal features.

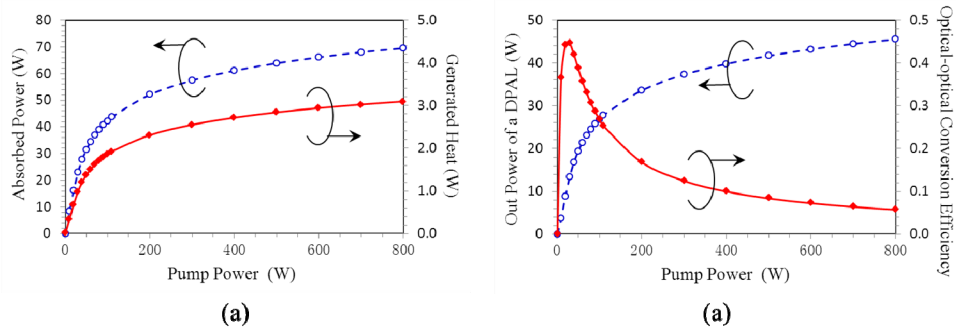

Fig. 11. Absorbed power and generated heat versus the pump power (a). Optical-optical conversion efficiency and laser output power versus the pump power (b).

4. Conclusion

Until now, the temperature inside the vapor cell has been considered as a constant in most of the literatures of DPALs. Actually, it is impossible completely eliminate the temperature gradient of a heated gas-state medium because of its small thermal conductivity. Since the saturated density of the alkali vapor is strongly dependent on the temperature, the kinetics process should be taken into account during evaluating the thermal characteristics. In this study, we developed a scheme by using both the heat transfer and the laser kinetics to analyze the temperature distribution inside an enclosed vapor cell. In our theoretical model, a cell is segregated to many coaxial cylindrical annuli. The population density and temperature in every cylindrical annulus have been finally calculated. It is seen that the temperature in the center of a vapor cell is higher than the other places at the cross section. The temperature gradient becomes serious with increase of the pump intensity. However, unlike some of the solid-state lasers, a stronger pump power does not always result in a higher optical-optical conversion efficiency for a DPAL. To solve such a problem, one of the effective methods to achieve a high-powered DPAL might be adopting a flowing-gas system. The thermal effects should be dramatically decreased by using such a dynamic procedure. The mathematical model will be much more complicated than that used in this report. In fact, the theoretical model in this paper can also be applied to the other two types of DPALs if the D_1 and D_2 radiative lifetimes, the pump absorption cross section, the collisionally-broadened cross section, and the thermally averaged relative velocities are changed to the new values corresponding to rubidium and potassium.

Additionally, the temperature distribution will inevitably bring about some changes in refractive index with temperature dn/dT. Decreasing the thermally-induced wave front distortion and thermal lensing effects should be important in realization of a DPAL with high beam quality. We will also introduce our results on this issue afterwards.

#210310 - $15.00 USD Received 18 Apr 2014; revised 18 May 2014; accepted 18 May 2014; published 30 May 2014

Acknowledgments

We are very grateful to Prof. Salman Rosenwaks and Dr. Boris D. Barmashenko at Ben-Gurion University of the Negev of Israel for their valuable helps in calculation of saturated alkali number densities inside a static alkali vapor cell.

#210310 - $15.00 USD Received 18 Apr 2014; revised 18 May 2014; accepted 18 May 2014; published 30 May 2014